IET Control Theory & Applications

Research Article

IET Journals
The Institution of Engineering and Technology

Stabilisation of grid assistance for a renewable hydrogen generation system by min-projection strategy

ISSN 1751-8644
Received on 12th December 2014
Revised on 24th July 2015
Accepted on 1st November 2015
doi: 10.1049/iet-cta.2014.1327
www.ietdl.org

José Gabriel García Clúa[1,2,3] ✉, *Ricardo J. Mantz*[1,4], *Hernán De Battista*[1,3], *Norma G. Gallegos*[2,5]

[1] *Instituto LEICI, Facultad de Ingeniería, Universidad Nacional de La Plata, C.C.91 (1900) La Plata, Argentina*
[2] *Departamento de Ingeniería Química, Facultad de Ingeniería, Universidad Nacional de La Plata, Argentina*
[3] *Consejo Nacional de Investigaciones Científicas y Técnicas (CONICET), Argentina*
[4] *Comisión de Investigaciones Científicas de la Provincia de Buenos Aires (CICpBA), Argentina*
[5] *Centro de Investigación y Desarrollo en Ciencias Aplicadas (CINDECA-CCT-CONICET) (1900) La Plata, Argentina*
✉ *E-mail: jose.garciaclua@ing.unlp.edu.ar*

Abstract: Control of grid assistance is proposed in this study for a renewable hydrogen generation system of simple and robust structure. Here, the grid connection serves the dual purpose of minimising the effect of wind power variations in the electrolyser supply as well as maximising the hydrogen production. To regulate the electrolyser current at its rated value, a cascade control scheme is posed. The feedback loop which commands the grid converter switching is of interest for the design. The min-projection strategy that stabilises a switched affine system is applied as the switching law. The analysis of switched equilibria and their stability is done by employing the concepts of Filippov inclusion and common Lyapunov function, respectively. The obtained theoretical results are corroborated by numerical simulation.

1 Introduction

Hydrogen generated by water electrolysis supplied with renewable energy sources may become a sustainable alternative to fossil fuels [1, 2]. This option is proving to be economically feasible thanks to progressive reduction in costs of wind and solar technologies [3, 4]. A renewable hydrogen generation system (RHGS) mainly produces hydrogen from renewable sources to be stored in applications such us H_2 fueling station [5, 6]. It can be classified according to the nature of the renewable power, the type of internal integration of its main components and the external dependence on the electric grid [7, 8]. Wind-powered RHGSs are one of the most convenient options, among other reasons, because of the reduced electricity costs of the wind turbines [9]. Since electrolysers have not been conceived to operate under the short-term and seasonal variability of the wind resource, special care must be taken when coupling both components [10].

In this work, a grid connected wind-based RHGS is considered. As can be seen in the scheme of Fig. 1, the electrolyser is directly coupled to a DC bus while the wind generator is connected to it by means of a diode rectifier [11]. The main advantages of this topology are the low maintenance and operating costs of the electronics. On the other hand, its main drawback is the lack of controllability of the rectifier. This fact can be compensated for with the assistance of the grid, if it is available. Negative effects on the electrolyser power quality caused by the variability of wind energy can also be mitigated by suitable power exchange with the grid [12, 13]. DC-bus voltage fluctuations caused by short-term power imbalances can be smoothed by properly controlling the DC-bus voltage and adding, if necessary, large capacitors or supercapacitors [14]. Another advantage of grid connection exploited in this paper is that electrolyser efficiency can be optimised despite wind variations. Since H_2 production rate is proportional to charge transfer flow, i.e. to electric current, H_2 production is maximised by maintaining the electrolyser current (i_E) at its rated value. Due to the direct coupling of the electrolyser to the DC bus, the proposed assistance strategy meets this condition by regulating the bus voltage (u_E) at the rated voltage of the electrolyser [10]. In this hydrogen production application, regulation of the DC-bus voltage is a critical point since the electrolyser current is very sensitive to voltage fluctuations.

A cascade control structure is considered here for this task. Its main objective is to reject the disturbance introduced by the renewable resource that can be modelled as a non-linear function of wind speed v as was described in a previous work [15]. The cascade control comprises an outer controller that computes the reference for the inner controller, being common practice to design the inner loop much faster than the outer one to avoid undesirable interactions and instability. The outer controller, that determines the grid current reference for the inner controller, can be designed using classical control design tools. It is therefore of particular interest in this application to design an inner controller as fast as possible so that the cascade control bandwidth can be designed high enough to reject the wind disturbance. Whereas classical control design is appropriate to synthesise the outer controller, switched control tools are exploited here to command the converter current i_C. This control design task is formulated as the stabilisation problem of a switched system that describes the converter dynamics [16, 17]. Unlike other works, here the design and analysis of the proposed stabilisation strategy is based on the application of common Lyapunov function (CLF) [18, 19] and Filippov inclusion [20] to the switched system. This rigorous theoretical framework is very useful to design the ideal strategy that a practical implementation should approach.

2 Model and control scheme for the RHGS

Fig. 2 depicts a simplified equivalent circuit of the wind-based RHGS schematised in Fig. 1. The DC-bus voltage dynamics (1) is governed by the current Kirchhoff law

$$\frac{\mathrm{d}u_E}{\mathrm{d}t} = \frac{1}{C}\left(i_R - i_E + i_C\right). \tag{1}$$

The power contribution of the wind turbine can be modelled as a voltage-dependent current source i_R that is function also of the

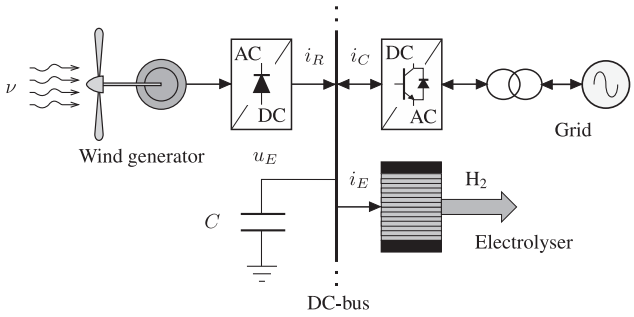

Fig. 1 *Grid-assisted wind-based RHGS*

rotational speed Ω and, indirectly, of wind speed v, according to the following expression

$$i_{\mathrm{R}} = \frac{1}{L_G}\left(\sqrt{3}\Phi - \frac{\pi u_{\mathrm{E}}}{3p\Omega}\right), \tag{2}$$

where L_G, Φ and p are, respectively, the synchronous inductance, the concatenated magnetic flux and the number of magnetic pole pairs of the permanent-magnet generator [15].

The electrolyser can also be modelled as a current source i_{E} with non-linear output resistance. The current–voltage characteristic is appropriately described by the function

$$u_{\mathrm{E}} = h\,(i_{\mathrm{E}}) = n\left[U_{\mathrm{rev}} + \frac{r_{\mathrm{e}}}{A} i_{\mathrm{E}} + s_{\mathrm{e}} \ln\left(\frac{t_{\mathrm{e}}}{A} i_{\mathrm{E}} + 1\right)\right], \tag{3}$$

where n is the number of electrolytic cells in series, U_{rev} is the reversible cell voltage, A is the electrode area and $\{r_{\mathrm{e}}, s_{\mathrm{e}}, t_{\mathrm{e}}\}$ are empirical coefficients that depend on the electrolyte temperature [15].

The three ideal selector switches depicted in Fig. 2 model the converter that implements the grid assistance i_{C} [21]. Depending on the renewable energy source, the grid may supply or absorb power. The AC side of the electronic converter is connected to the grid through a filter. This filter is devoted to smooth the grid side currents i_k. Finally, the grid is modelled as a star-connected three-phase sinusoidal voltage source e_k – with peak voltage $\hat{E}$ and angular frequency ω – in series with the grid inductance.

Fig. 3 shows the control scheme that regulates the DC-bus voltage to the rated value U_{E}^N, regardless of the wind variations that directly affect i_{R}. By (3), U_{E}^N is set to fix the electrolyser current to its rated value I_{E}^N that maximises the hydrogen production. The proposed DC-bus control consists of two feedback loops in cascaded configuration. The outer loop controller ($\mathcal{C}_{\mathrm{E}}$) input is the DC-bus voltage error $U_{\mathrm{E}}^N - u_{\mathrm{E}}$ while its output is the set of reference grid currents $i^{\star}_{\{dq\}}$ for the inner controller ($\mathcal{C}_{\mathrm{I}}$). This controller regulates the grid currents by a suitable switching strategy for the AC/DC converter. In the design of both controllers, two separate time scales exhibited by the RHGS dynamics are considered. The slower time scale is associated with the DC-bus dynamics and control, which are designed to smooth the imbalances caused by the wind power fluctuations in the wind turbulence spectrum (up to

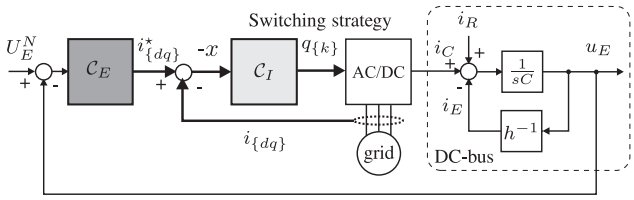

Fig. 3 *Control scheme of the grid–assisted RHGS*

1 Hz approximately). The faster time scale is associated with the grid currents dynamics and control since the AC filter is designed to attenuate the switching frequency of the converter. The synthesis of $\mathcal{C}_{\mathrm{E}}$ can be solved using classical tools of continuous control theory like in [11]. Instead, the synthesis of $\mathcal{C}_{\mathrm{I}}$ is treated in this paper with hybrid nature analysis tools taking account of the interaction between continuous and discrete states inherent to converter operation. This controller design method is developed in detail in the following section.

3 Grid currents control design

3.1 Dynamic model of the AC-side currents

The k-phase converter leg is commanded by the switching signal $q_k \in \{0, 1\}$ as shown in Fig. 2. The switch connects the phase k to the positive DC-terminal when $q_k = 1$, and to the negative DC-terminal when $q_k = 0$. All combinations of three-switches positions are associated with a discrete state that takes values according to the following binary-to-decimal conversion

$$q = 2^2 q_2 + 2^1 q_1 + 2^0 q_0, \tag{4}$$

i.e. $q \in \{0, 1, \ldots, 7\}$. The combination corresponding with $q = 1$ is represented in Fig. 2. The remaining seven combinations correspond with many other variants of the same circuit structure.

On the other hand, the continuous current dynamics is mainly governed by the AC filter. For the sake of clarity in the presentation, a series L filter is considered to derive the dynamics equations. However, this model is still valid for LCL filters [22] after some changes in notation.

By solving the aforementioned discrete variants, the following continuous dynamics associated with each value of q are obtained [16]

$$\frac{\mathrm{d}i_{\{k\}}}{\mathrm{d}t} = \frac{1}{L} e_{\{k\}} - \frac{2}{3L} u_{\mathrm{E}} M q_{\{k\}}, \tag{5}$$

where $i_{\{k\}} = [i_0 \quad i_1 \quad i_2]^{\mathrm{T}}$ is the continuous state vector; $e_{\{k\}} = [e_0 \quad e_1 \quad e_2]^{\mathrm{T}}$ is the continuous input vector; $q_{\{k\}} = [q_0 \quad q_1 \quad q_2]^{\mathrm{T}}$ is the binary representation of the discrete state q; and

$$M = \begin{bmatrix} 1 & -\frac{1}{2} & -\frac{1}{2} \\ -\frac{1}{2} & 1 & -\frac{1}{2} \\ -\frac{1}{2} & -\frac{1}{2} & 1 \end{bmatrix}. \tag{6}$$

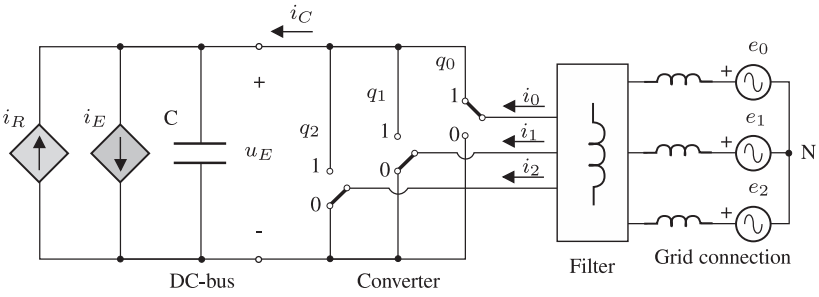

Fig. 2 *Simplified circuit of the grid assistance at DC-bus side*

IET Control Theory Appl., 2016, Vol. 10, Iss. 2, pp. 183–189

In (5), L represents the sum of the series filter inductance and the inner inductance of the transformer that couples the converter to the grid connection point [23]. In the case of an LCL filter (5) is still valid with L being the converter-side inductance of the filter and $e_{\{k\}}$ being the phase voltage at the terminals of the filter capacitor.

Finally, DC-side i_C and AC-side $i_{\{k\}}$ converter currents are related by means of the equation

$$i_C = q_{\{k\}}^T i_{\{k\}}. \tag{7}$$

For control purposes, it is more convenient to represent all three-phase variables $z_{\{k\}} = [z_0\ z_1\ z_2]^T$ in the synchronous d–q reference frame $z_{\{dq\}} = [z_d\ z_q]^T$ by means of the transformation

$$A_{dq}^k = \frac{2}{3}\begin{bmatrix} \cos(\theta) & \cos\left(\theta-\frac{2\pi}{3}\right) & \cos\left(\theta+\frac{2\pi}{3}\right) \\ -\sin(\theta) & -\sin\left(\theta-\frac{2\pi}{3}\right) & -\sin\left(\theta+\frac{2\pi}{3}\right) \end{bmatrix}, \tag{8}$$

with $\theta = \omega t$. In the new frame, (5) becomes

$$\frac{di_{\{dq\}}}{dt} = A_\omega i_{\{dq\}} + \frac{1}{L}\left(e_{\{dq\}} - u_E\, q_{\{dq\}}\right) \tag{9}$$

where

$$A_\omega = \omega\begin{bmatrix} 0 & 1 \\ -1 & 0 \end{bmatrix}. \tag{10}$$

Active and reactive powers flowing through the grid lines, represented in d–q coordinates, are

$$p_C = \frac{3}{2}\left(e_d i_d + e_q i_q\right), \tag{11}$$

$$q_C = \frac{3}{2}\left(e_d i_q - e_q i_d\right), \tag{12}$$

respectively.

3.2 Stabilisation by min-projection strategy

The inner controller aims to track the reference grid currents $i^\star_{\{dq\}}$. Then, the dynamics (9) can be conveniently rewritten in terms of the current error

$$x = i_{\{dq\}} - i^\star_{\{dq\}}, \tag{13}$$

as follows

$$\dot{x} = f_q(x,\theta) = A_\omega x + b_q(\theta), \tag{14}$$

where

$$b_q(\theta) = A_\omega i^\star_{\{dq\}} + \frac{1}{L}e_{\{dq\}} - \frac{1}{L}u_E\, q_{\{dq\}}. \tag{15}$$

and $i^\star_{\{dq\}}$, provided by the slow outer controller is assumed to be practically constant. Therefore, the regulation objective of $\mathcal{C}_I$ involves the stabilisation of (14). That is, the switching strategy must satisfy the steady state $x^\star = 0$. This cannot be achieved with any of the discrete states q from (14) because their equilibrium points

$$f_q(x_q^*,\theta) = 0 \quad \Leftrightarrow \quad x_q^* = A_\omega^{-1} b_q(\theta) \tag{16}$$

depend on the time-variant parameter θ, and usually they are not null. It means switching between linear subsystems is a necessary condition to reach and stay in a neighbourhood of $x^\star$, which is called 'switched equilibrium' [24].

For stabilisation of switched system (14) the following switching logic is proposed

$$q^\star = \arg\left\{\min_{q\in\mathcal{Q}} x^T f_q(x,\theta)\right\}, \tag{17}$$

which is known as minimum projection strategy or min-projection [25, 26]. Indeed, for each pair $(x,\ \theta)$ it selects a value $q^\star$ of the discrete state q such that the projection of the field $f_{q^\star}$ over x is actually minimised. By replacing (14) into (17) yields

$$q^\star = \arg\left\{\min_{q\in\mathcal{Q}} x^T\left(A_\omega x + b_q(\theta)\right)\right\} \tag{18}$$

The minimisation problem is solved by analysing the q-dependent term of (18). That is

$$\min_{q\in\mathcal{Q}}\left\{x^T b_q(\theta)\right\} = \min_{q\in\mathcal{Q}}\left\{-\frac{1}{L}u_E x^T q_{\{dq\}}\right\}. \tag{19}$$

The argument of (19) is developed to determine the negativity of the scalar product. Thus, positive factors are neglected

$$-x^T q_{\{dq\}} = q_{\{k\}}^T\left(A_{dq}^k\right)^T(-x) = \sum_{k=0}^{2} q_k\, g_k\,(x,\theta). \tag{20}$$

It is observed in this sum that each scalar term

$$g_k\,(x,\theta) = \frac{2}{3}x_2 \sin\left(\theta - \frac{2k\pi}{3}\right) - \frac{2}{3}x_1\cos\left(\theta - \frac{2k\pi}{3}\right) \tag{21}$$

is commanded with the corresponding binary signal q_k and that its sign depends on the pair $(x,\ \theta)$. So the minimum of (20) is achieved by the combination $q^\star_{\{k\}}$ which adds the terms g_k only when they are negative. This means that, for all k, the following must be satisfied

$$g_k\,(x,\theta) < 0 \Rightarrow q_k^\star = 1, \tag{22}$$

$$g_k\,(x,\theta) \geq 0 \Rightarrow q_k^\star = 0. \tag{23}$$

The switching conditions (22) and (23) can be expressed with the matrix sign function

$$\text{sign}\left(g_{\{k\}}\right) = \begin{bmatrix}\text{sign}(g_0) & \text{sign}(g_1) & \text{sign}(g_2)\end{bmatrix}^T \tag{24}$$

in order to obtain the explicit dependence on continuous states of the switching vector

$$q^\star_{\{k\}} = \begin{bmatrix}\frac{1}{2} & \frac{1}{2} & \frac{1}{2}\end{bmatrix}^T - \frac{1}{2}\text{sign}\left\{\left(A_{dq}^k\right)^T(-x)\right\}. \tag{25}$$

Finally, the scalar discrete state $q^\star$ that solves the minimisation problem (18) is obtained by replacing the vector (25) into (4).

3.3 Stability of the switching law $q^\star$

Let V be the quadratic function

$$V(x) = \frac{1}{2}x^T x, \tag{26}$$

it can be shown that min-projection strategy minimises the derivative of V, by substituting (17) into

$$\dot{V} = \dot{V}_{q^\star} = x^T f_{q^\star}(x,\theta) = \min_{q\in\mathcal{Q}}\left\{\dot{V}_q\right\}. \tag{27}$$

However, the minimisation of $\dot{V}$ does not guarantee its negativity for all $x \in \mathcal{D}om(q^\star)$. That is the property that V must satisfy to be a CLF candidate of a stable switched system [18]. In particular, the

exponential stability of system (14) under the switching law (17) must satisfy

$$x^{\mathrm{T}}\left(A_{\omega}x + b_{q^{\star}}(\theta)\right) \leq -cx^{\mathrm{T}}x \quad \forall x \in \mathcal{D}om(q^{\star}), \tag{28}$$

where c is a positive constant. By substituting (15) into (28) and rewriting in terms of the vector $\bar{v}$, it is obtained

$$x^{\mathrm{T}}\underbrace{\left(cx + A_{\omega}i_{\{dq\}} + \frac{1}{L}e_{\{dq\}} - \frac{1}{L}u_{\mathrm{E}}\,q_{\{dq\}}\right)}_{\bar{v}} \leq 0. \tag{29}$$

Condition (29) is interpreted geometrically in the x_1–x_2 plane of Fig. 4. There $\bar{v}$ is depicted as the resultant of its vector components. The vector component corresponding to the first term of the sum given in (29) is always collinear to x. That corresponding to second and third terms is made collinear to consider the worst $i_{\{dq\}}$ and $e_{\{dq\}}$ combination. Finally, the vector coming from the discrete term of the sum admits the following phasor representation as a function of q_k

$$-\frac{1}{L}u_{\mathrm{E}}q_{\{dq\}} \equiv \frac{2}{3L}u_{\mathrm{E}}\sum_{k=0}^{2} q_k\, e^{-j(\theta - 2\pi k/3 - \pi)}. \tag{30}$$

The relative position of phasors (30) as a function of q is shown in Fig. 4. Note that phasors corresponding to $q = 0$ and $q = 7$ have zero magnitude, while the remaining ones lie in a circle of radius $2u_{\mathrm{E}}/3L$ and rotate clockwise with velocity $\dot{\theta} = \omega$. For instant $t = 0$ considered θ is such that the minimum $x^{\mathrm{T}}\bar{v}$ is zero, either by selecting the phasor '$q = 1$' or '$q = 5$'. Note that the right triangle formed with the latter phasor implies the following equality

$$c^{*}\|x\| + \left\|A_{\omega}i_{\{dq\}} + \frac{1}{L}e_{\{dq\}}\right\| = \frac{2}{3L}u_{\mathrm{E}}\cos\left(\frac{\pi}{6}\right), \tag{31}$$

where c^{*} is the upper bound of c. Applying (31) to the inequality $0 < c < c^{*}$ leads to the condition

$$\left(i_d - \frac{e_q}{\omega L}\right)^2 + \left(i_q + \frac{e_d}{\omega L}\right)^2 < \left(\frac{u_{\mathrm{E}}}{\omega L\sqrt{3}}\right)^2, \tag{32}$$

which shows the inside of a circle in the d–q plane. It represents the region of the converter operation where the proposed control is exponentially stable. A limiting case of this stability is corroborated in Fig. 4, where x represents a point $i_{\{dq\}}$ near the boundary of region (32). Note that always exists a $c > 0$, however, small it may be as $i_{\{dq\}}$ approaches the boundary, such that the direction of the vector field $f_{q^{\star}}$ guides the state trajectory $x(t)$ to the origin.

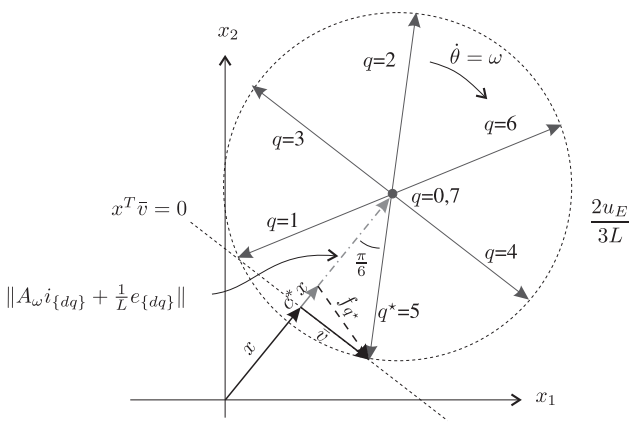

Fig. 4 *Geometric interpretation of stability*

3.4 Equilibrium in the Filippov sense

The switched equilibrium $x^{\star} = 0$ reached when $q = q^{\star}$ switching law is applied can be interpreted by reformulating the switching system (14) as the Filippov differential inclusion $\dot{x} \in F(x)$ [20], where

$$F(x) = \mathrm{co}\left\{f_q\right\}_{q\in\mathcal{Q}} \triangleq \sum_{q=0}^{7}\alpha_q f_q, \tag{33}$$

$$\alpha_q \geq 0 \quad \forall q \in \mathcal{Q}, \tag{34}$$

$$\sum_{q=0}^{7}\alpha_q = 1. \tag{35}$$

It is noted that this analysis is more powerful than that in the frequency domain requiring a single small-signal transfer function. By substituting (33) and (14) into the equilibrium condition $F(x^{\star}) = 0$, it yields

$$\sum_{q=0}^{7}\alpha_q\left(-\frac{1}{L}u_{\mathrm{E}}q_{\{dq\}}\right) = -A_{\omega}i^{\star}_{\{dq\}} - \frac{1}{L}e_{\{dq\}}. \tag{36}$$

whereas the phasors of the convex combination corresponding to $q = 0$ and 7 are null, and that corresponding to $q = 6$, 5 and 3 are, respectively, opposite to those related to $q = 1$, 2 and 4 (see Fig. 4), equality (36) is expressed in the following matrix form

$$\frac{1}{L}u_{\mathrm{E}}A^{k}_{dq}\begin{bmatrix}\alpha_6 - \alpha_1\\ \alpha_5 - \alpha_2\\ \alpha_3 - \alpha_4\end{bmatrix} = \frac{2u_{\mathrm{E}}}{3L}\rho\begin{bmatrix}\cos\varphi\\ \sin\varphi\end{bmatrix}, \tag{37}$$

where ρ and φ denote, respectively, the magnitude and angle phase of the right-hand side of (36) regardless of the variable θ. The Filippov coefficients α_q satisfying (37) for all θ are proposed below

$$\begin{aligned}
&\alpha_0 = \alpha_7 = 0,\\
&\alpha_1 = \alpha(\theta - \varphi - \pi), \quad \alpha_4 = \alpha\left(\theta - \varphi - \frac{\pi}{3}\right),\\
&\alpha_2 = \alpha\left(\theta - \varphi + \frac{\pi}{3}\right), \quad \alpha_5 = \alpha\left(\theta - \varphi - \frac{2\pi}{3}\right),\\
&\alpha_3 = \alpha\left(\theta - \varphi + \frac{2\pi}{3}\right), \quad \alpha_6 = \alpha(\theta - \varphi),
\end{aligned} \tag{38}$$

where $\alpha(\cdot)$ is the even periodic function

$$\alpha(\theta) = \frac{a_0}{2} + \sum_{n=1}^{\infty} a_n\cos(n\theta). \tag{39}$$

From conditions (35) and (37) satisfied by the Filippov coefficients α_q it can be proved that the following Fourier coefficients result

$$a_0 = \frac{1}{3}, \tag{40}$$

$$a_1 = \frac{1}{3}\rho, \tag{41}$$

$$a_{6m} = a_{6m\pm1} = 0. \tag{42}$$

That is, harmonics of order multiple of six and their contiguous must have Fourier coefficients null. The rest are chosen to meet (40), (41) and (34). The value assumed by the coefficient ρ is directly dependent on this choice. The maximum ρ can be extracted from (37) evaluated in $\theta = \pi/6$ and $\varphi = 0$ without loss of generality

$$\begin{bmatrix}\frac{\sqrt{3}}{2} & 0 & -\frac{\sqrt{3}}{2}\\ -\frac{1}{2} & 1 & -\frac{1}{2}\end{bmatrix}\cdot\begin{bmatrix}\alpha\left(\frac{\pi}{6}\right) - \alpha\left(\frac{5\pi}{6}\right)\\ 0\\ \alpha\left(\frac{5\pi}{6}\right) - \alpha\left(\frac{\pi}{6}\right)\end{bmatrix} = \begin{bmatrix}\rho\\ 0\end{bmatrix}. \tag{43}$$

IET Control Theory Appl., 2016, Vol. 10, Iss. 2, pp. 183–189

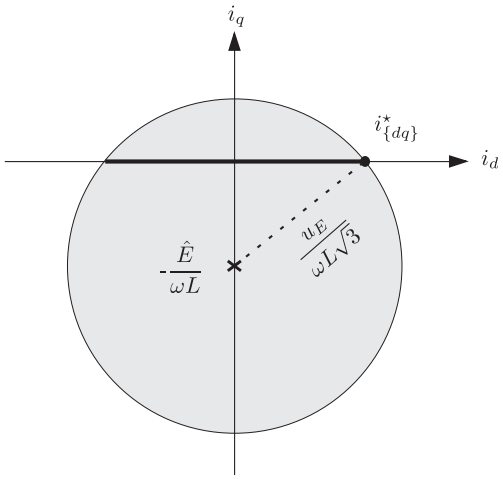

Fig. 5 *Operation region of the grid converter*

Indeed, if the restriction (34) – equal to $\alpha(\theta) \geq 0\ \forall\theta$ – as well as the restriction (35) are both added to (43), then the maximum ρ results

$$\rho_{\max} = \frac{\sqrt{3}}{2}, \tag{44}$$

such that it satisfies

$$\alpha\left(\frac{\pi}{6}\right) = \frac{1}{2} \quad \text{and} \quad \alpha\left(\frac{\pi}{2}\right) = \alpha\left(\frac{5\pi}{6}\right) = 0. \tag{45}$$

The evaluation of (37) in $\rho_{\max}$ gives the following bound for the right-hand side of (36)

$$\left\| A_\omega i^\star_{\{dq\}} + \frac{1}{L} e_{\{dq\}} \right\| \leq \frac{2u_{\rm E}}{3L}\rho_{\max} = \frac{u_{\rm E}}{\sqrt{3}L}, \tag{46}$$

which is consistent with the stability condition (31) applied to the steady state ($x = 0$). As a consequence, the desired switched equilibrium $i^\star_{\{dq\}}$ must belong to the region (32), which matches the linear zone of the space-vector pulse-width modulated (SVPWM) technique [27]. Outside this region there is no choice of coefficients a_n to satisfy the Filippov inclusion and over modulation arises.

The converter operation region is represented in Fig. 5 for the case of e_{r0} aligned with the d-axis – i.e. $e_d = \hat{E}$ and $e_q = 0$ – whereby $p_{\rm C}$ (11) and $q_{\rm C}$ (12) become dependent on i_d and i_q, respectively. Therefore, the reactive power exchange between the converter and the grid can be cancelled out by setting to zero the coordinate $i^\star_q$ in the set-point of $\mathcal{C}_{\rm I}$. The active power can be regulated varying the other coordinate within the range

$$|i^\star_d| \leq \frac{1}{\omega L}\sqrt{\frac{1}{3}u_{\rm E}^2 - \hat{E}^2}, \tag{47}$$

as long as the design condition

$$u_{\rm E}/\hat{E} > \sqrt{3} \tag{48}$$

is satisfied. The maximum value of $|i^\star_d|$ arises from the intersection of the operation region with the d-axis which is represented in bold in Fig. 5.

4 Simulation results

This section is aimed at verifying the stability characteristics of the proposed controller $\mathcal{C}_{\rm I}$ by numerical simulation of a grid-assisted wind-RHGS. This consists of a 100 kW wind turbine, an alkaline electrolyser with rated current $I_{\rm E}^N = 200$ A and rated voltage $U_{\rm E}^N = 271$ V, and a grid converter with the same power as the electrolyser. Critical operation condition for which the RHGS requires maximum grid assistance to maintain H_2 generation at rated values is considered. In this case, the control reference should be such that $p_{\rm C} = I_{\rm E}^N \cdot U_{\rm E}^N$ and $q_{\rm C} = 0$. By replacing in (47) the parameters

$$u_{\rm E} = U_{\rm E}^N, \quad e_{\{dq\}} = [110\sqrt{2} \quad 0]^{\rm T}\ \text{V and}\ \omega L = 73\,\text{m}\Omega \tag{49}$$

it is obtained

$$i^\star_{\{dq\}} = [230\ 0]^{\rm T}\ \text{A}. \tag{50}$$

Such a point belongs to the region (46) because the relation $u_{\rm E}/\hat{E} = 1.9$ satisfies (48).

Fig. 6 displays in the d–q plane a set of state trajectories of the system controlled by the minimum projection strategy. Such trajectories allow to verify the asymptotic stability of the switched equilibrium $i^\star_{\{dq\}}$. The trajectory highlighted in bold illustrates the critical stability situation analysed in (31) with $c^* = 0$. The time evolution of this trajectory is shown in Fig. 7. It can be seen how grid currents reach and hold the desired values (50) after a finite time τ of the order of the period $T = 2\pi/\omega$. However, it is noted that τ will not be the settling of the voltage $u_{\rm E}$, which will evolve to reach its rated value ($U_{\rm E}^N$) according to the slower DC-bus dynamics. This is commanded by the outer loop controller ($\mathcal{C}_{\rm E}$) as shown below in another simulation. Furthermore, it should be

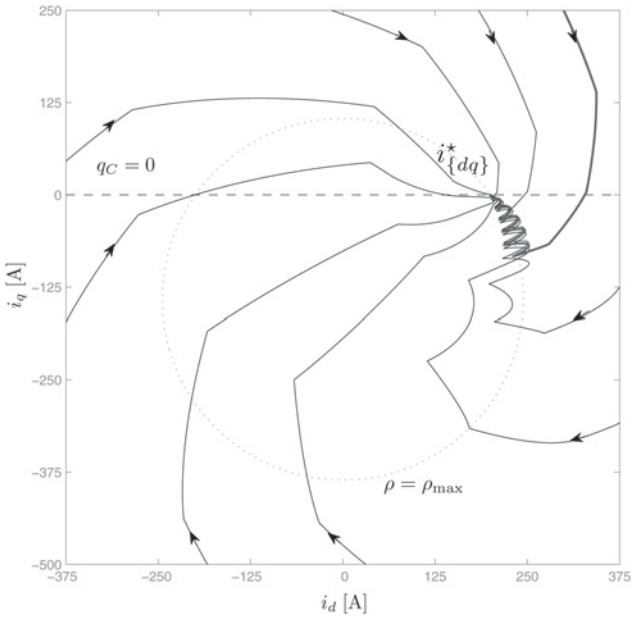

Fig. 6 *Grid currents trajectories*

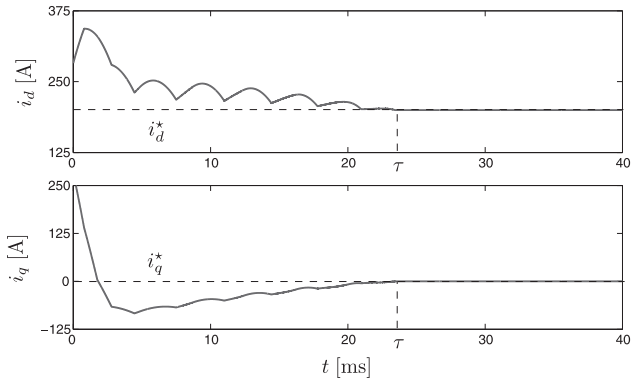

Fig. 7 *Time response of a critical grid currents trajectory*

clear that the significant overshoot observed in the time response is due to the initial condition outside the circle established as operating region of the converter. Although stability isguaranteed even for initial conditions outside the limit of the linear modulation of the SVPWM technique, in practice it is not convenient to work in over modulation because the need to maintain grid synchronisation.

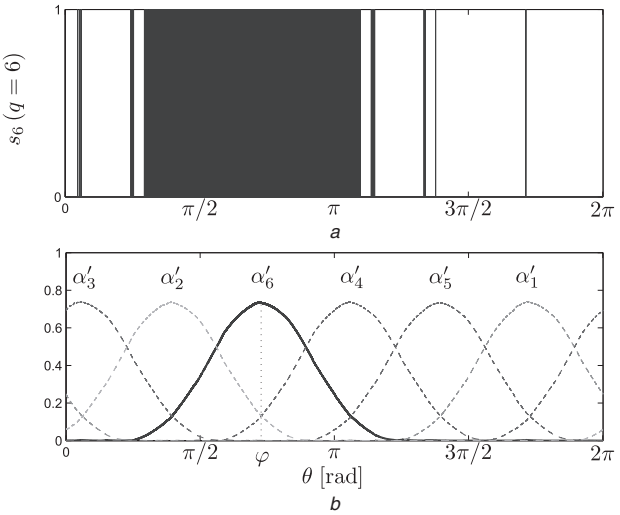

Fig. 8 *Filippov inclusion that keeps invariant the switched system state*
a Activation signal related to the state $q = 6$
b Filtered signal which matches the coefficient α_6

Table 1 Simulated and theoretical characteristic values

θ	$\pi/6$	$\pi/2$	$5\pi/6$
$\alpha'(\theta)$	0.49	0.01	0.00
$\alpha(\theta)$	0.5	0	0

To verify characteristics of the Filippov inclusion that keeps the state of the switched system (14) invariant in $i^{\star}_{\{dq\}}$, the high frequency switching signal s_6 shown in Fig. 8*a* is analysed in one grid cycle. This signal reports the activation instants of the state $q = 6$. Note that the theoretical stabilisation at this switched equilibrium point requires ideal commutation at infinite frequency. For practical implementation, the switching frequency can be limited as in practical sliding mode control. In our simulations, an hysteresis was incorporated to limit the switching frequency at 13 kHz maximum. It can be seen in Fig. 8*b* that curve α'_6 resulting from the filtering of signal $s_6(t)$ is the Filippov coefficient corresponding to the discrete state $q = 6$. According to (38), $\alpha_6(\theta)$ equals $\alpha(\theta)$ with the offset phase angle φ. Then the Fourier series expansion is applied to $\alpha'(\theta) = \alpha'_6(\theta + \varphi)$, which returns the coefficients $a'_0 = 0.33$, $a'_1 = 0.28$ and $a'_5 = a'_6 = a'_7 = 0.00$. These match a_n given in (40)–(42) with $\rho = \rho_{\max}$. Moreover, $\alpha'(\theta)$ evaluated at the characteristic angles reported in Table 1 approximates to the theoretical values specified in (45) for $\rho = \rho_{\max}$. The remaining Filippov coefficients α_q may be verified by following a similar procedure from the filtered signals α'_q of Fig. 8*b*.

As anticipated above, simulation results showing the performance of the overall system are included below. To give an idea of how the proposed strategy affects the outer control loop in the cascaded scheme, a simple proportional–integral controller was applied in $\mathcal{C}_{\mathrm{E}}$. The adjustment method was based on a linear model of the RHGS that deserves a detailed treatment as given in [11]. Fig. 9 shows the time response of DC-bus variables and grid currents for a rotational speed profile generated by the turbine. It verifies a satisfactory DC-bus voltage regulation even at low levels of the renewable source. This affects directly the hydrogen production through the electric characteristic (3).

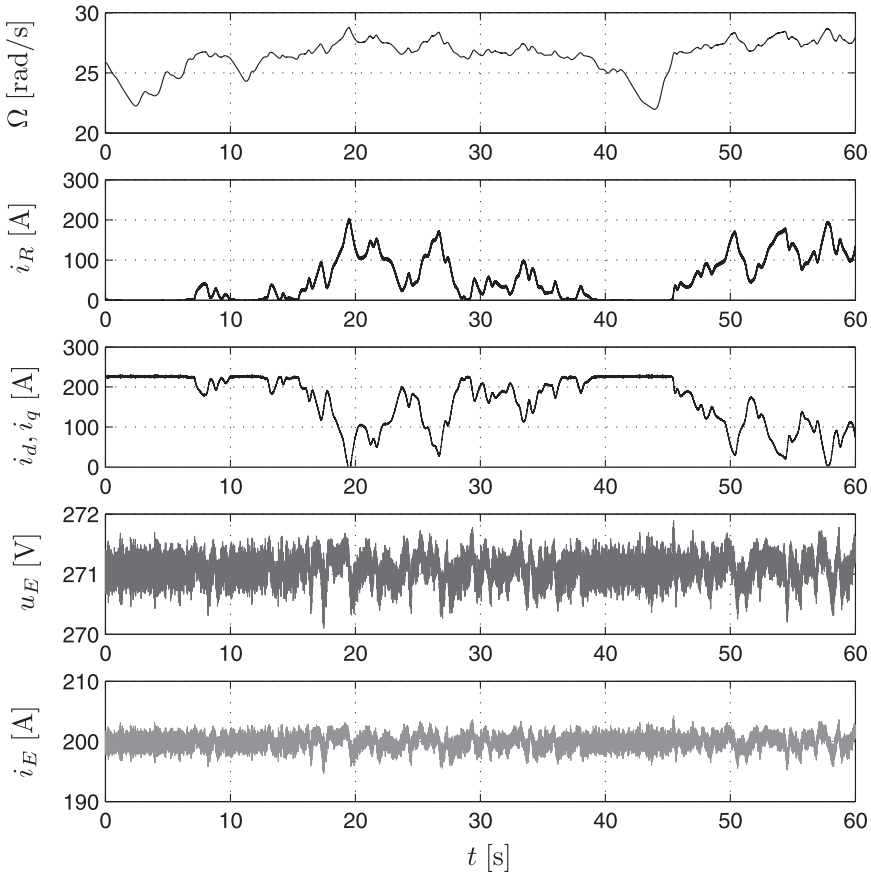

Fig. 9 *Time response of the DC-bus dynamics for a rotational speed profile generated by the turbine*

IET Control Theory Appl., 2016, Vol. 10, Iss. 2, pp. 183–189

5 Conclusions

The grid assistance control proposed for a particular wind-RHGS maximises H_2 production regardless of wind power fluctuations. In the implemented cascade control scheme, the inner feedback loop dedicated to grid currents regulation is of special interest. The designed controller follows the outer loop reference by switching between six discrete states of the grid-side converter. The switched affine system presented as a RHGS model comes from the analysis of the continuous dynamics associated with each discrete state in the framework d–q. The proposed switching strategy for system stabilisation was based on minimum projection or *Min-Projection* technique, whose main attractiveness lies in its simple interpretation and application from an engineering point of view. Thanks to that technique, proof of exponential stability based on CLF could be interpreted geometrically inside a circle of the d–q plane. Also, switched equilibrium analysis by Filippov differential inclusions could be linked with the indicated interpretation. Convex combination coefficients returning the desired equilibrium were determined by Fourier series whose fundamental frequency is that of the grid. As a result of theoretical analysis and numerical simulations, similarities between *Min-Projection* and SVPWM techniques have been detected.

6 Acknowledgments

This work was funded by ANPCyT, CONICET, CICpBA and UNLP of Argentina.

7 References

1 Ursúa, A., Gandía, L., Sanchis, P.: 'Hydrogen production from water electrolysis: current status and future trends', *Proc. IEEE*, 2012, **100**, (2), pp. 410–426
2 Tzamalis, G., Zoulias, E., Stamatakis, E., *et al.*: 'Techno-economic analysis of an autonomous power system integrating hydrogen technology as energy storage medium', *Renew. Energy*, 2011, **36**, (1), pp. 118–124
3 Erdinc, O., Uzunoglu, M.: 'Optimum design of hybrid renewable energy systems: overview of different approaches', *Renew. Sustain. Energy Rev.*, **16**, 2012, (3), pp. 1412–1425
4 Olateju, B., Monds, J., Kumar, A.: 'Large scale hydrogen production from wind energy for the upgrading of bitumen from oil sands', *Appl. Energy*, 2014, **118**, pp. 48–56
5 Deshmukh, S.S., Boehm, R.F.: 'Review of modeling details related to renewably powered hydrogen systems', *Renew. Sustain. Energy Rev.*, 2008, **12**, (9), pp. 2301–2330
6 Neves, N.P., Pinto, C.: 'Licensing a fuel cell bus and a hydrogen fueling station in Brazil', *Int. J. Hydrog. Energy*, 2013, **38**, (19), pp. 8215–8220
7 Zhou, T., Francois, B.: 'Energy management and power control of a hybrid active wind generator for distributed power generation and grid integration', *IEEE Trans. Ind. Electron.*, 2011, **58**, (1), pp. 95–104
8 Pedrazzi, S., Zini, G., Tartarini, P.: 'Modelling and simulation of a wind-hydrogen {CHP} system with metal hydride storage', *Renew. Energy*, 2012, **46**, pp. 14–22
9 Genc, G., Celik, M., Genc, M.S.: 'Cost analysis of wind-electrolyzer-fuel cell system for energy demand in Pinarbasi–Kayseri', *Int. J. Hydrog. Energy*, 2012, **37**, (17), pp. 12158–12166
10 Sarrias-Mena, R., Fernández-Ramírez, L.M., García-Vázquez, C.A., *et al.*: 'Electrolyzer models for hydrogen production from wind energy systems', *Int. J. Hydrog. Energy*, 2015, **40**, (7), pp. 2927–2938
11 García-Clúa, J., De Battista, H., Mantz, R.: 'Control of a grid-assisted wind-powered hydrogen production system', *Int. J. Hydrog. Energy*, 2010, **35**, (11), pp. 5786–5792
12 Sherif, S., Barbir, F., Veziroglu, T.: 'Wind energy and the hydrogen economy-review of the technology', *Sol. Energy*, 2005, **78**, pp. 647–660
13 Jørgensen, C., Ropenus, S.: 'Production price of hydrogen from grid connected electrolysis in a power market with high wind penetration', *Int. J. Hydrog. Energy*, 2008, **33**, (20), pp. 5335–5344
14 Díaz-González, F., Sumper, A., Gomis-Bellmunt, O., *et al.*: 'A review of energy storage technologies for wind power applications', *Renew. Sustain. Energy Rev.*, 2012, **16**, (4), pp. 2154–2171
15 García-Clúa, J., Mantz, R., De Battista, H.: 'Evaluation of hydrogen production capabilities of a grid-assisted wind-h2 system', *Appl. Energy*, 2011, **88**, (5), pp. 1857–1863
16 Utkin, V., Guldner, J., Shi, J.: 'Sliding mode control in electromechanical systems' (Taylor and Francis, London, 1999, 1st edn.)
17 Alsmadi, Y., Utkin, V., Xu, L.: 'Sliding mode control of ac/dc power converters', Fourth Int. Conf. on Power Engineering, Energy and Electrical Drives (POWERENG), 2013, pp. 1229–1234
18 Liberzon, D.: 'Switching in systems and control' (Birkhäuser, Boston, 2003)
19 Xu, L., Wang, Q., Li, W., *et al.*: 'Stability analysis and stabilisation of full-envelope networked flight control systems: switched system approach', *IET Control Theory Appl.*, 2012, **6**, (2), pp. 286–296
20 Filippov, A. F.: 'Differential equations with discontinuous righthand sides', 1988.
21 Bose, B.: 'Power electronics and AC drives' (Prentice-Hall, 1986)
22 Yoon, D.-K., Jeong, H.-G., Lee, K.-B.: 'The design of an lcl-filter for the three-parallel operation of a power converter in a wind turbine', IEEE Energy Conversion Congress and Exposition (ECCE), 2010, pp. 1537–1544
23 Chinchilla, M., Arnaltes, S., Burgos, J.: 'Control of permanent-magnet generators applied to variable-speed wind-energy systems connected to the grid', *IEEE Trans. Energy Convers.*, 2006, **21**, (1), pp. 130–135
24 Bolzern, P., Spinelli, W.: 'Quadratic stabilization of a switched affine system about a nonequilibrium point', Proc. 2004 American Control Conf., 2004, vol. 5, pp. 3890–3895
25 Pettersson, S., Lennartson, B.: 'Stabilization of hybrid systems using a min-projection strategy', Proc. 2001 American Control Conf., 2001, vol. 1, pp. 223–228
26 Wang, M., Zhao, J.: 'Quadratic stabilization of a class of switched nonlinear systems via single Lyapunov function', *Nonlinear Anal. Hybrid Syst.*, 2010, **4**, (1), pp. 44–53
27 Mirafzal, B., Saghaleini, M., Kaviani, A.: 'An svpwm-based switching pattern for stand-alone and grid-connected three-phase single-stage boost inverters', *IEEE Trans. Power Electron.*, 2011, **26**, (4), pp. 1102–1111